Journal of Power Sources 665 (2026) 239053

Contents lists available at ScienceDirect

Journal of Power Sources

journal homepage: www.elsevier.com/locate/jpowsour

In-depth analysis of the SEI thickness growth over the lifetime of Li-ion cells from an automotive battery

Franziska Allgayer [a,b], Markus H. Hofmann [a], Helmut Ehrenberg [b], Mathias Storch [a], Fabian Jeschull [b,*]

[a] Mercedes-Benz AG, Mercedesstraße 120, 70372, Stuttgart, Germany
[b] Karlsruhe Institute of Technology (KIT), Institute for Applied Materials (IAM), Hermann-von-Helmholtz Platz 1, 76344, Eggenstein-Leopoldshafen, Germany

HIGHLIGHTS

- In-depth SEI analysis of automotive cells at different aging stages.
- XPS depth profiling analysis to track compositional changes at different states of health.
- Transmission electron microscopy analysis on electrode cross-sections.
- Simplified lab-scale electrode setup for more efficient growth rate parameterization.
- Comparison of SEI growth rates at electrode centre and edge regions for future modelling activities.

GRAPHICAL ABSTRACT

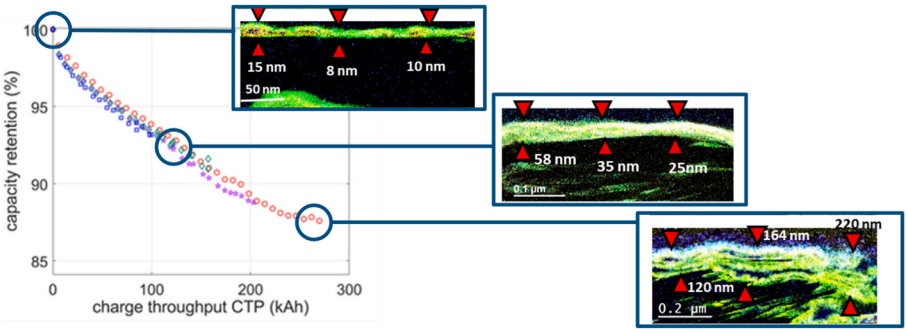

ARTICLE INFO

Keywords:
Automotive lithium-ion cells
SEI growth rate
XPS
EELS/EDS
Formation/ reaction kinetics
Electrolyte reduction

ABSTRACT

Developing a detailed understanding of the ageing evolution in automotive lithium-ion cells is key to batteries with long service life. In this study, the SEI composition and growth rate of graphite negative electrodes from cycle-aged large-format automotive lithium-ion cells is investigated as important parameters in physics-based ageing models. In this work, automotive cells were cycle-aged in a duty cycle protocol with intermittent reference parameter test. The SEI layers formed at different state-of-health were characterized by X-ray photoelectron spectroscopy sputter depth profiling and electron microscopy on electrode cross-sections. The SEI growth over time showed a linear relationship. However, the growth rates derived from the two techniques differed considerably and major differences in SEI thicknesses were found between edge and center regions of electrode sheets. In an attempt to facilitate access to relevant experimentally derived model parameters, a lab-scale setup build from Li-ion cell components from an automotive battery was developed that could reproduce the SEI evolution and growth behavior.

* Corresponding author.
E-mail address: fabian.jeschull@kit.edu (F. Jeschull).

https://doi.org/10.1016/j.jpowsour.2025.239053
Received 20 August 2025; Received in revised form 21 November 2025; Accepted 4 December 2025
Available online 6 December 2025

1. Introduction

Lithium-ion batteries are the most expensive component in electric vehicles and their degradation is a multifaceted challenge for reliable lifetime prediction [1]. The challenge lies in the complexity stemming from the interplay of numerous factors, including cell design (e.g., electrode materials, formulations, balancing, etc.) [2–4], electrolyte composition [5], cell form factors [6] and storage or operation conditions (such as temperature [7,8]or depth of discharge (DoD) [9,10]). These variables influence the ageing behavior and failure modes, making it difficult to generalize degradation trends across different battery systems [1,11,12]. Within the product development cycles, accelerated ageing tests at elevated stress levels, e.g. test at elevated temperatures, that increase the degradation rate are inevitable during this phase. This then poses the challenge to transfer and extrapolate the results to the unaccelerated testing case [13,14]. Application-driven testing, particularly in the case of automotive cells, leads to additional layers of complexity, taking into account for instance duty cycles (instead of charge-discharge cycles at constant current densities), temperature fluctuations (in field tests), as well as calendar ageing times (vehicle stand idle ca. 96 % of the time) [14,15]. In particular in the case of automotive cells, path dependencies are difficult to replicate in a laboratory environment. Long-term, unaccelerated cycling studies under controlled thermal environments thus are complementary and critical for quantifying and classifying ageing behaviours and failure modes, as well as validating end-of-life predictions [16]. Using real-world usage profiles delivers detailed insights into how stress factors like temperature, DoD, and cycling rate interact over time, enabling more accurate lifetime modelling and improved battery management strategies [12]. On a more fundamental level there are two major types of degradation pathways associated with the loss of active material (LAM) and the loss of lithium inventory (LLI) [8]. LAM includes processes related to damages to active material or electrode coating, e.g. graphite exfoliation or particle cracking; while LLI refers to processes that consume lithium-ions, especially electrolyte degradation or Li plating. Depending on the prevailing type of battery ageing, the ageing trajectory the capacity retention is characterized either by linear or sublinear (i.e. decay-type) capacity loss *vs.* cycle number, while superlinear/non-linear ageing trajectories are characterized by a slower capacity decay over most of the battery's lifetime before a rapid decay sets in [17].

The deposition of degradation products forms a passivating film that mitigates continued electrolyte degradation upon further cycling, known as the solid electrolyte interphase (SEI). The SEI is first formed during the cell conditioning on the first cycles when electrolyte components decompose at the negative electrode interface at low potentials. The SEI is a heterogeneous layer that comprises of both inorganic and organic compounds, specifically LiF and Li_2CO_3 that are typically located near to the electrode surface ('inner SEI') as well as carbonyl- and ether-based organic compounds found in the outer regions [18–20]. Cracks in the surface layer and SEI re-formation leads to continuous loss of mobile Li inventory and, overall a growth of the SEI layer thickness. This is reflected in capacity fade and increasing internal resistance [21–23].

Both parameters are important for the training of (semi-)empirical, physics-based ageing models for the lifetime predictions of automotive cells [11,24–26]. They are linked by the formation and growth of the SEI layer and hence, detailed knowledge of the SEI characteristics under different ageing conditions is a prerequisite for accurate modelling approaches. Previously introduced four-parameter models attribute capacity fade to the SEI layer growth, which is ascribed to either LAM at the anode, and cathode, or LLI from irreversible reactions at the electrode interfaces [16,26,27]. This model gives a base framework for the data-driven approach. To minimize interfering effects at the experimental level, e.g. pressure changes, change in thermal conditions or state of charge (SoC), only one of the operating conditions was changed for each cell testing. We correlate electrochemical signatures like capacity retention, resistance profiles and differential voltage analysis (DVA) to results from surface-analytical techniques, namely X-ray photoelectron spectroscopy (XPS) and a combination of the transmissions electron microscopy mapping (TEM) with electron energy loss spectroscopy (EELS) and energy-dispersive X-ray spectroscopy (EDS). The method gives detailed information on the chemical composition within the probing volume of the surface layer, and allows quantification of the respective elemental concentrations and relative ratios between chemical species [28–30]. However, its probing depth becomes a limiting factor for cells aged for a long time, as the surface layer thickness can exceed the probing depth of the technique, unless sputter [28] or synchrotron-based depth profiling is applied [4,31]. Additional information can be obtained from complementary TEM-EELS/EDS experiments on electrode cross-sections, which allows to conveniently extract the surface layer thickness and adds spatial resolution with regards to the elemental distribution in the electrode-SEI surface region. With this combined set of data, the elemental distribution of SEI components, their chemical nature and the SEI layer thickness are extracted, thus providing a detailed picture of the surface layer as an experimental basis for lifetime prediction studies and an approach to determine SEI growth rates [29,30,32–34].

2. Experimental

Cell characteristics. The following study is based on an extensive cycling ageing test comprising 63 automotive-grade Li-ion pouch cells with a nominal capacity of 43 Ah. The cells arrived pre-cycled from the manufacture. The outer dimension of the cells are 16.5 cm:16 cm:3 cm (l x w x h) and comprise of graphite as the negative electrode and a blend of $Li(Ni_{0.6}Mn_{0.2}Co_{0.2})O_2$ and $Li(Ni_{1/3}Mn_{1/3}Co_{1/3})O2$ on the positive electrode. The areal capacity of the graphite electrodes were determined in a previous work by Stadler et al. [35] with the same automotive cell type. The mean initial capacity (determined experimentally) was 2.71 ± 0.20 mAh cm^{-2} on the full-cell and 2.87 ± 0.01 mAh cm^{-2} on half cell level. The electrode-separator stack is z-folded using a PE-PP layered separator. The electrolyte contained ethylene carbonate (EC) and diethyl carbonate (DEC) with $LiPF_6$ as electrolyte salt.

Experimental Setup (Cell Tests). For long-term testing the cells were braced (Fig. S1) in between two steel-jigs (2, 3) with nickel-chromium alloy springs (spring constant 36 N/mm) to provide a force of ~1.1 kN throughout the complete test. Additionally, a 1.8 cm thick steel plate together with load cells is implemented below the cell-plate sandwich (1 and 2) to continuously monitor the force deviation over test time (min 0.5–5 kN, accuracy <0.5 %). The load cells are arranged with equal distance to the center of the steel plates. On the top, a 0.5 cm thick steel plate together with a displacement gauge (4) in the center position S1 (min range: 0–5 mm, resolution: 10 nm) is mounted for continuous monitoring of the cell thickness. Thermoelements are deployed between the two cell tabs (S2) and in the climate chamber to track cell and ambient temperature. The expansion of the cell was measured at the Begin of Test (BoT) and the End of Test (EoT) at open circuit voltage (OCV_{max}).

Ageing Test – Automotive Cells. The ageing tests are described the following parameters: temperature (T), maximum SoC (SoC_{max}), minimum SoC (SoC_{min}), charging power (P_{CH}) and driving power profile (Fig. 1a). The cells were heated to a constant temperature of 30 °C in a temperature chambers (Vötsch, Weiss Technik, Germany) prior to cycling. The cells were kept stored at 0 % SoC and 25 °C for 14 days before the start of the ageing test in order to equalize inhomogeneities and reduce the effect of reversible capacity changes by the overhang effect [36]. A schematic of the measurement steps are shown Fig. 1b. The ageing test comprised of duty cycles based on a power charge/discharge profile from an electrical vehicle (EV) drive profile. Intermittent reference parameter tests (RPT) were conducted every two weeks to determine the state-of-health of the automotive cells [37].

In the duty cycles, charging was conducted with a constant power -

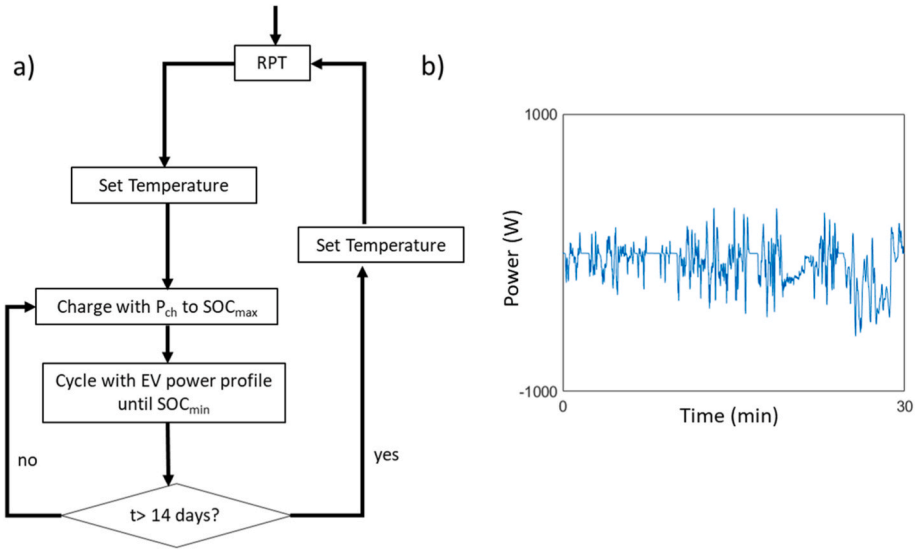

Fig. 1. a) Schematic of the duty cycle/intermittent RPT test procedure: a repeating power charge/discharge profile was applied for 14 days. The test is then interrupted for an RPT cycling profile to test state of the cells electrochemically, before the cells are send into another 14 day duty cycle sequence. B) Illustration of the EV drive profile applied upon discharge to SoC_{min} [12].

constant voltage protocol (CP-CV), applying a constant charge power of P_{ch} = 136 W until SOC_{max} of 90 % is reached. In the discharge sequence, a power profile was applied until SoC_{min} (30 %) is reached (Table 1) [37]. This test cycle was repeated for 14 days, after which RPT was performed. The RPTs were carried out at 25 °C and comprised of a first cycle at a constant current of 1C (C = actual/nominal cell capacity) with the voltage limits of 2.5–4.2 V. After 1 h of voltage relaxation at 100 % SoC a discharge pulse of 200 A for 10 s was applied to determine the internal resistance of the cells (Fig. 1a). The C/10 discharge capacity obtained from the regular RPT tests was used for the calculation of the (cumulative) charge throughput (CTP in kAh) at the end of each 14 days test cycle. For the evaluation of the differential voltages, the potential curve is derived from the C/10 discharge step with respect to the charge (dV/dQ). For the test in automotive cells, five different states of ageing were defined based on the CTP: the begin of test (BoT) describes a cell prior to cycling, CTP = ~100 kAh (mid of test 1; MoT1), ~150 kAh (mid of test 2; MoT2), ~200 kAh (mid of test 3; MoT3) and, end of test (EoT), is defined as CTP = ~280 kAh.

Ageing Tests – Three-Electrode Cells. In an attempt to transfer the test of automotive cells onto lab scale cells, lithium-ion cells were assembled in a three-electrode PAT-Cell (EL-Cell GmbH, Germany) setup.

Cell Assembly. For the electrode preparation, the automotive cells (BoT cells) are disassembled to extract the electrode sheets. The electrodes are removed from the center of the electrode stack (layer 10th to 20th) and washed to remove residual electrolyte (such as conductive salt). One coated side of electrode is mechanically removed with dimethyl carbonate and Cyrene™ (Merck, Germany). Then electrode discs with a diameter of 18 mm were cut from the positive and negative electrode sheets.

The cell stack comprised a copper plunger, the graphite negative electrode, an insulation sleeve (ECC1-00-0210-V/X, EL-Cell GmbH, Germany) with Li-reference electrode and Viledon FS2226E (PP fiber) and Lydall Solupore 5P09B (PE membrane) separators (220 µm), the NMC positive electrode and an aluminum plunger [38]. The separators were soaked in 110 µL electrolyte (base electrolyte of the automotive cells; provided by the cell supplier) [38]. The cells were cycle at 30 °C and subjected to a formation procedure with C/3 cycles. This step was necessary for sufficient wetting of the freshly filled electrolyte with the already cycled extracted electrodes from the automotive cells.

Cell Testing. The test on three-electrode cell level follows the same procedure as the automotive cells with a power profile scaled to the lower capacity of the thus prepared cells. To reach a long-term stability the temperature chambers were purged with inert gas (N_2) to reduce interferences from moisture and oxygen entering the cell compartment. The cells were cycled on a CTS battery cycler (BaSyTec GmbH, Germany). The charge throughput of the three-electrode labscale cells was determined as aforementioned for the automotive cells (see above). An equivalent charge throughput was defined as a means to compare CTPs between automotive and three-electrode cells. The conversion factor of 1.5 (from labscale to automotive cell) was derived from the comparison of the energy throughputs of lab-scale and automotive cells and translated to the corresponding CTP. For the lab-scale cells, the MoT state (for SEI studies) is then defined as 50 'equivalent kAh' that is an early ageing stage to gain first insights of SEI characteristics. The cells were cycled between a SoC between 10 and 70 %. The charge rate was set to 1C to adapt the P_{ch} of the pouch cell level (Table 1). The charge limits for the three-electrode cells are already set in the testing system.

Post-Mortem Analysis. For the following *post-mortem* analysis all cells were discharged after their designated ageing time, to a cell voltage of 3 V using a constant discharge current of 3.7 A, which ensured similar SoC of all samples as a common basis for comparison. The cells were then opened under inert atmosphere in an Argon-filled glovebox (O_2 and H_2O levels below 0.1 ppm). The procedure involves dissembling the cells and the electrodes of the stack are separated and removed from the center of the electrode stack from 15th to 18th layer of the aged automotive cells (MoT1, MoT2, MoT3, EoT cells). Then they are washed in dimethyl carbonate (Merck KGaA, Germany) in ca. 200 mL for 3 min to remove the conductive salt residues. After drying, photographs of representative electrodes of each cell are taken and the electrodes are stored until further analysis [39].

X-Ray Photoelectron Spectroscopy. XPS measurements are carried

Table 1
Overview of the operation conditions of the automotive and three-electrode cells. The charge for the three-electrode cells is given by the C-rate. Charge limits are already implemented in the testing system.

	SoC_{min} (%)	SoC_{max} (%)	Charge Condition	Temperature (°C)
automotive cell	30	90	136 W	30
three-electrode cell	10	70	1 C	30

out on a K-alpha spectrometer (Thermo Fisher Scientific, United States) equipped with a glovebox compartment for inert gas transfer. The sample preparation was conducted in an Ar-filled glovebox, and the transfer between the glovebox and spectrometer are handled without any air exposure. A monochromized Al Kα X-ray source is used with the excitation energy of 1486.6 eV. A pass energy of 50 eV is used for both survey and detailed spectra. On each sample several measurements spots were defined to confirm reproducibility. An argon ion gun is used for sputter depth profiles with an etching rate of 0.52 nm s^{-1} (referred to Ta_2O_5) at an energy of 3 keV. The photoemission spectra were recorded after sputter times of 30, 60, and 180 s. The data was analyzed in "Avantage" (Thermo Fisher Scientific, United States). For background subtraction, the "smart background" function was used (Shirley background with an additional constraint that the background function is not greater than any datapoint in the measured region). A fitting model was first developed for the BoT sample and the peak positions and peak shapes adapted to data of aged electrodes as initial parameters for the curve fits. For consistency the binding energy boundaries of the individual peak components were fixed within a narrow, predefined range. This was feasible as no major deviations from the starting parameters was observed (nor were they expected). Quantification of the elemental distribution of the surface layer, as shown in Table 2, was performed based on the ratio of the normalized peak area to the sum of all normalized total peak areas correlating to 100 at.%, taking into account the instrument-specific sensitivity factors.

Electron Microscopy. The electrode surfaces of graphite electrodes from differently cycle-aged cells were studied by scanning electron microscopy (SEM), before the preparation of cross-section specimens. Then a protective Pt/C layer of was deposited on the sample to mitigate surface damage. Cross-sectioning and preparation of FIB-cut lamella was performed by a focused ion beam (FIB) with a gallium sputter source and then attached to a TEM grid. TEM was used for the structural and compositional characterization of the SEI. The samples were transferred to the TEM chamber under inert gas atmosphere to avoid any exposure to ambient air or moisture. The analysis conducted in a spherical aberration-corrected transmission electron microscope JEOL ARM200F (JEOL, Japan) with a probe corrector (CEOS GmbH, Germany) at 200 kV. The microscope is equipped with a cold-field emission gun in conjunction with the EELS (Gatan Quantum ERS, United States). In this study, electron energy loss spectroscopy (EELS) and energy-dispersive X-ray spectroscopy (EDS) are used to detect the elements Li1s, F1s, O1s and P2p. The intensities of the P2p and F1s signals are weak and also fluorine signals displayed an overlap with the Li1s signal, leading to the use of EDS as the more sensitive detection method for these two elements.

Table 2
Peak Positions of the C1s, O1s, F1s and P2p regions in the BoT, MoT1 and EoT. The binding energy boundaries were fixated.

Core Level	Compounds	binding energy	BoT	MoT1	MoT2	MoT3	EoT
		eV	at.%	at.%	at.%	at.%	at. %
C1s	sp^2-C/ graphite	284.4	5.5	1.0	0.0	0.0	1.6
	$-CH_2-/sp^3$-C	285	12.4	24.0	21.5	21.3	19.6
	-CO-	286.7	1.0	6.1	6.6	7.3	2.9
	-(C=O)O-	288.9	1.2	1.6	2.9	4.0	1.3
	-O(C=O)O-	289.9	0.8	3.4	2.3	3.2	1.5
O1s	Li_2O	528.0	<0.5	<0.5	<0.5	<0.5	3.0
	C=O	531.4	22.9	27.2	22.2	30.1	22.8
	-CO-	533.3	1.7	2.5	3.2	4.8	1.4
F1s	LiF	685	9.0	4.8	2.0	1.9	6.1
	$(O=P)F_x(OR)_y$	687.4	0.7	1.9	1.7	3.3	–
P2p	$O=PF_x(OR)_y$ ($2p_{3/2}$)	133.3	2.3	1.4	1.2	1.3	1.6
	P-S ($2p_{3/2}$)	132	0.7	–	–	–	–
Li1s	Li^+	55.4	35.3	24.5	21.9	22.5	37.0

[§]C=O (carbonyl groups) include carboxyl groups (-(C=O)O-) and carbonate groups (-O(C=O)O-).

3. Results

3.1. Ageing and post-mortem analysis of automotive cells

In this first section, the degradation of automotive cells in a duty-RPT test was evaluated over an extended testing period. Underlying degradation processes, such as the evolution of the SEI surface layer thickness, were studied in a detailed post-mortem analysis leveraging complementary surface analytical techniques on aged electrode sheets at different state-of-health (SoH).

Cell Aging and Electrochemical Evaluation. The automotive cells were subjected to a duty cycle/intermittent reference parameter test (for details see *Experimental Section*) until the desired charge throughput (CTP) limit was reached. The state-of-health was determined from a combination of capacity retention, and normalized internal resistance as a function of CTP, as well as from differential voltage analysis (DVA) curves generated from the RPT sequences, as shown in Fig. 2.

Capacity Retention. In Fig. 2a the capacity fade *vs.* charge throughput is shown for the four different ageing stages MoT1 (red), MoT2 (green), MoT3 (purple) and EoT (blue), following the testing procedure described above. Each data point represents the mean value of two cells. The capacity fade between each set of samples is well reproducible until the cells reached their targeted CTP stop criteria. A maximum capacity loss of ~13 % was measured after CTP = 280 kAh (EoT) with a small deviation of only ± 0.2 % between the two samples.

Internal Resistance. Fig. 2b shows the evolution of the change in internal resistance (relative to the value at BoT in %) as a function of CTP. In the CTP range from 0 to 150 kAh the resistance is smaller than the initial values measured for the BoT cell. After 150 kAh, the resistance is gradually increasing, followed by a steep increase by about 10 % over a narrow CTP range from 250 to 280 kAh. The sudden change from a constant to an increasing resistance hints towards underlying ageing effects that become significant after extended cycle-ageing tests. The onset of a 'resistance elbow' is an indication of the cell entering a superlinear decay [15].

Differential Voltage Analysis (DVA). In Fig. 2c the differential voltages analyses (DVA, dV/dQ) are shown for the MoT1, MoT2 and MoT3 ageing stages. The color gradient indicates the number of RPT check-ups from blue (first measurement) to red (last measurement). All cells display an initial capacity of around 43 Ah, in agreement with Fig. 2a. As outlined by Sieg et al. [38], the two dominant peaks, GII (at ca. 4.6 Ah) and GIII (at ca. 25.6 Ah), in the DVA represent phase transitions in the graphite voltage profile [40].

With increasing state of ageing the peaks undergo gradual changes, as their intensity diminishes, the peak centers shift on the capacity axis. A measure for the relative changes is the difference between the two peak maxima, Δ(GIII- GII), which increases from 21.1 Ah to 22.1 Ah. The change is accompanied by peak broadening and shallower local minima of dV/dQ [41]. It further shows that upon aging the two intercalation plateaus are affected to different degrees, with the second plateau experience stronger changes. This effect is ascribed to a dispersion of the different degrees of lithiation between individual graphite particles in the electrode composite [10,42]. In other words, the lithiation process of the graphite electrode becomes increasingly heterogeneous the longer the cell cycles, i.e. the peak changes over the ageing test of MoT1 are minor, compared to the changes in cells (MoT2 and MoT3) that cycle-aged for longer times (passed through more test cycles). The heterogenous distribution of the lithiation during ageing has a significant impact on the electrode capacities. The decrease of the capacity can be attributed to LLI caused by the SEI layer growth. The loss of available lithium results in a gradual shift in the cell balancing, which

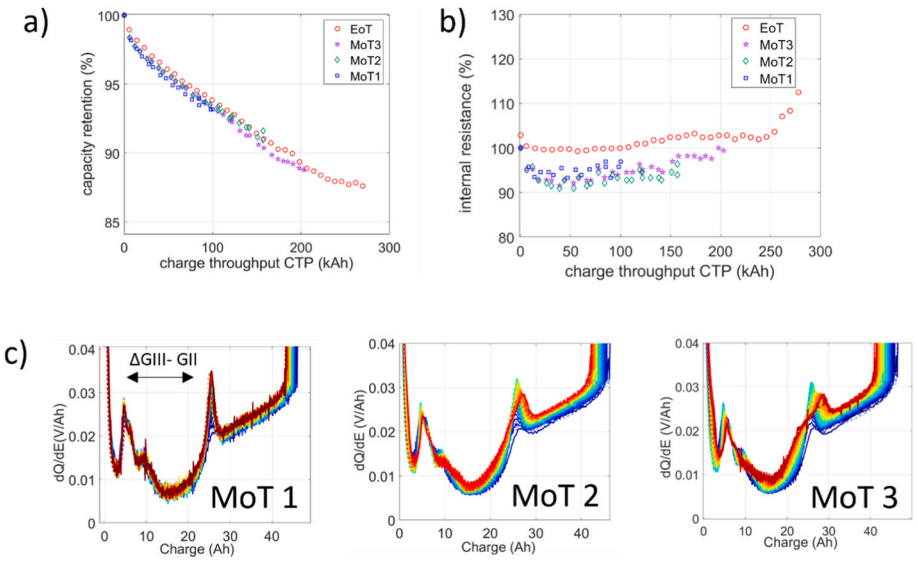

Fig. 2. a) Capacity retention *vs.* CTP for differently aged samples (MoT1-3 and EoT) and b) corresponding internal resistance *vs.* CTP. c) Differential Voltage Analysis (DVA), dV/dQ *vs.* Charge (Q) for samples MoT1 to MoT3. The color gradient indicates the progressive RPT measurements every 14 days starting from the first RPT test (blue) to the last RPT test (red) of the respective cell (MoT1, MoT2 and MoT3). (For interpretation of the references to color in this figure legend, the reader is referred to the Web version of this article.)

in turn gives rise to further degradation processes (e.g. through shifts in the voltage window) [11,43–45].

Optical Changes during Ageing. The photographs show that at the beginning of ageing test the electrode shows a characteristic light-grey surface with randomly distributed brownish spots stemming from the formation cycles carried out by the manufacturer. With increasing CTP, the aged electrodes show a brown region in the center of the electrode sheet that increased from the BoT state to the MoT1 state. At longer ageing times (MoT1 and MoT2), the area first turns blue and gradually increases in size. The EoT cell also displayed a metallic-silver area in the electrode center, indicating lithium plating. The SEI growth appears to start mainly from the center of the electrode sheet, which will be further discussed below (XPS depth profiles). During ageing (Fig. S1), the characteristic blue colored centered area is expanding, and silver spots of lithium plating appear. Stadler et al. [11] linked the lithium plating to electrolyte dry out in the cell, which is consistent with the notable resistance increase observed in Fig. 2b as well with the growth of the blue spots. Eventually, the electrolyte dry-out is attributable to an increase of the internal heat, particularly in the center of the electrode stack. The reduced heat dissipation could be a consequence from the cell geometry, as suggested by temperature distribution modelling, e.g. by Kosch et al. [46], who demonstrated that the electrode edges are generally colder regions in the cell compared to the electrode center. Elevated cell stack temperatures may accelerate electrolyte dewetting and in turn, heterogeneous electrolyte distribution can amplify non-uniform electrode processes and side reactions (e.g. Li-plating). Moreover, it could be assumed that the blue coloration is the result of the intercalation stage III as reported by Shellikeri et al. [47] and suggests a possible inhomogeneous potential distribution across the electrode sheets [11,48]. For a more detailed analysis of the negative electrodes of the automotive and three-electrode cells XPS sputter depth profiling and EELS/EDS cross-section analysis are performed, which will be described in the following section.

X-ray Photoelectron Spectroscopy Analysis. To identify the degradation products on the electrode surface further chemical-physical analysis is performed. Based on the optical analysis of the electrode sheets above, the samples discussed in this section were extracted from center parts of the cell stacks. Photoemission spectra for C1s, O1s, F1s and P2p regions are presented in Fig. 3 for the BoT, MoT1 and EoT samples.

C1s-spectra. Carbon spectra in the binding energy (BE) range of 280–292 eV (Fig. 3a–c) cover the peaks of the graphite environment. The peak at around 283.3 eV is ascribed to graphite/sp^2-carbon species of carbon black and the graphite active material ('bulk signal'), while the peak of saturated hydrocarbon -CH_2-/sp^3-appears at 285 eV [49]. The peak at around 287 eV is assigned to CO-species. Carboxylate -((C=O)O)- species with -C=O- as carbonyl group are located at around 288.8 eV [29] and carbonates (-O(C=O)O-) appear at around 290 eV [30]. The C and O containing species (CO, -(C=O)O-, -O(C=O)O-) are indicative for SEI components and their intensity increases from BoT to EoT, i.e. with prolonged aging. The -CH_2-/sp^3-C content increases from 12.4 at.% at BoT to values between 19 and 24 at.% for the MoT1-MoT3, as well as the EoT samples (Table 2). At the same time, the graphite/sp^2-carbon signal decreases rapidly from the BoT state to the MoT1 state and disappears entirely for longer aging times but reappears as a minor feature in the EoT stage. This suggests overall that the SEI layer thickness increases during cycle aging, as expected. A slight broadening of the CO-signal is observed in MoT and EoT compared to BoT (Fig. 3b & c). The overall CO content increased from around 1 at.% to around 6 at.% in the MoT samples, but decreased again in the EoT sample to 3 at.%. Similarly, the –(C=O)O- increased from 1.2 at.% (BoT) to up to 4 at.% (MoT3). The -O(C=O)O- (carbonate) peak increased notably from BoT to MoT1, and showed lower relative contents for MoT2 and MoT3. Interestingly, in all cases relative surface contents of the SEI species decreased towards the EoT stage (Table 1). Previous studies by Lucht and coworkers [50] suggested that the SEI undergoes gradual changes from an early to an aged surface composition. Compounds such as lithium alkyl carbonates (such as lithium ethylene dicarbonate, LEDC) or Li_2CO_3 surface deposits are gradually converted (mediated by $LiPF_6$) into LiF and a range of other compounds, e.g. polyethers and fluorophosphates [31]. In addition, further reactions are suspected once the electrolyte starts to dry out in the late phase of the ageing process [51].

O1s spectra. In Fig. 3d–f the most intense peak is observed at around 531.6 eV and assigned to C=O group of both carbonates and carboxylates -(C=O)O- components, i.e. a main constituent in the SEI. Another weaker peak in the shoulder of the C=O-component towards higher binding energies, at around 533.4 eV, is ascribed to CO-species. The oxygen spectra in Fig. 3d–f shows a peak at 528 eV that is ascribed to Li_2O. The -(C=O)-species (with R being an alkyl-group, for instance R=CH_3) have the highest atomic distribution (Table 1). A peak at 528 eV

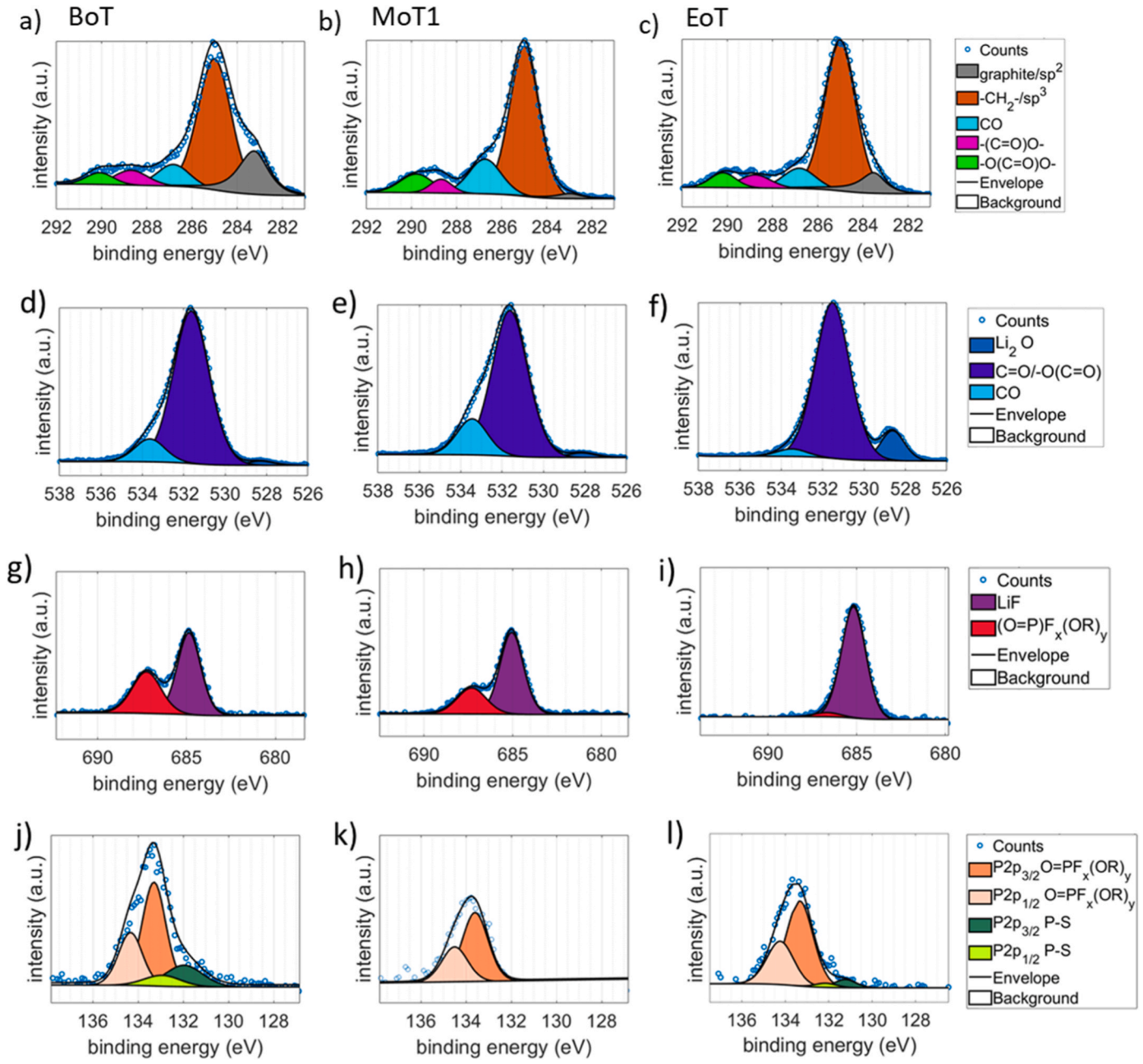

Fig. 3. C1s spectra (a–c) O1s spectra (d–f) F1s-spectra (g–i) P2p-spectra (j–l) are taken from the anode surfaces from BoT to EoT. The signals of the C1s-, O1s-, F1s- and P2p-species show the composition of the SEI over the stage of health. Some signals like LiF get broader or more prominent until End of Test.

suggests minor amounts of Li_2O. In the comparison between different stages of ageing the relative Li_2O peak intensity gradually increases. It is a species which already forms with very low content of water contained in the electrolyte [43].

F1-spectra. The fluorine species in Fig. 3g–I shows a strong LiF signal at around 685 eV. Moreover, a second signal is assigned to the P-F component of the related fluorophosphate species at around 687 eV. The LiF content decreases continuously from 9.0 at.% (BoT) to 1.9 at.% (MoT3). LiF is typically found in the 'inner' SEI layer, i.e. close to the graphite active material. When the surface layer is growing in course of ageing, in-house spectrometers rapidly encounter probing depth limitations. In the MoT1-MoT3 samples, the graphite peak is barely visible or not visible at all, meaning that neither the innermost sections of the SEI nor the electrode material beneath is seen in the photoemission spectra. Hence, the gradual decrease of the LiF signal is likely a result of SEI growth. As mentioned above, at EoT the surface composition changed notably, presumably due to other side reactions as the cell dries out. Under these conditions the LiF content increased again in the EoT sample to 6.1 at.% [21]. The residual compounds like the fluorophosphate-species only appear in the initial ageing states, i.e. prior to cycling (BoT) and at the MoT1 stage, when the electrode sheets are still well wetted with electrolyte.

P2p spectra. In the P2p phosphorous environments in Fig. 3j–l two phosphorous-containing degradation compounds are observed. Mono- and difluoroalkly phosphates ($O{=}PF_x(OR)_y$) (orange doublet) are observed at 133.4 eV ($P2p_{2/3}$). Fluoroalkyl phosphates are degradation products of the PF_6-anion with residual water or soluble dialkyl bis (ethylene carbonates) in the electrolyte [52]. In addition, a minor signal at around 131.1 eV ($P2p_{3/2}$) is seen in the spectra of BoT and EoT, is likely ascribed to phosphorous sulfides (green doublet) through interactions with sulfur-containing electrolyte additives in the electrolyte formulation (not further specified by the cell manufacturer) [53].

Within the scope of this study, the origin of the sulfur species was not further investigated (see Fig. S3). Interestingly, there was no indication of a PF_6^- signal in the P2p spectra, which is quite unusual [50]. With respect to the P-F signal in the F1s spectra, this would further suggest that the signal originates mainly from the degradation products $O{=}PF_x(OR)_y$. The surface concentration of degraded PF_6^- in the P2p and F1s spectra showed values around 1–3 at.% (Table 2), i.e. about equal amounts within the margin of error for this analysis (up to a few at.%). As already mentioned above, the absence of the PF_6^- signal could also be a result of a comparatively thick SEI layer. However, in this case one would expect a peak of this compound in the BoT sample [54].

In summary, the compositional changes of the SEI layer of cycle-aged automotive cells after selected stages of ageing was followed by *post-mortem* in-house XPS analysis. The data suggest that the surface layer grows notably between the BoT sample and the MoT1 sample, which is indicated by the notable decrease of the graphite signal in the C1s spectrum. The analysis thus may not capture the full composition of the surface layer under the applied measurement conditions, due to limitations in probing depth. This might be a reason for decreasing LiF levels, if the compound is part of an inner section of the layer that moves gradually outside the information depth of the technique with increasing layer thickness. To address this limitation, sputter depth profiling was performed in the following section as a means to receive more information on the inner sections of the surface layer. In

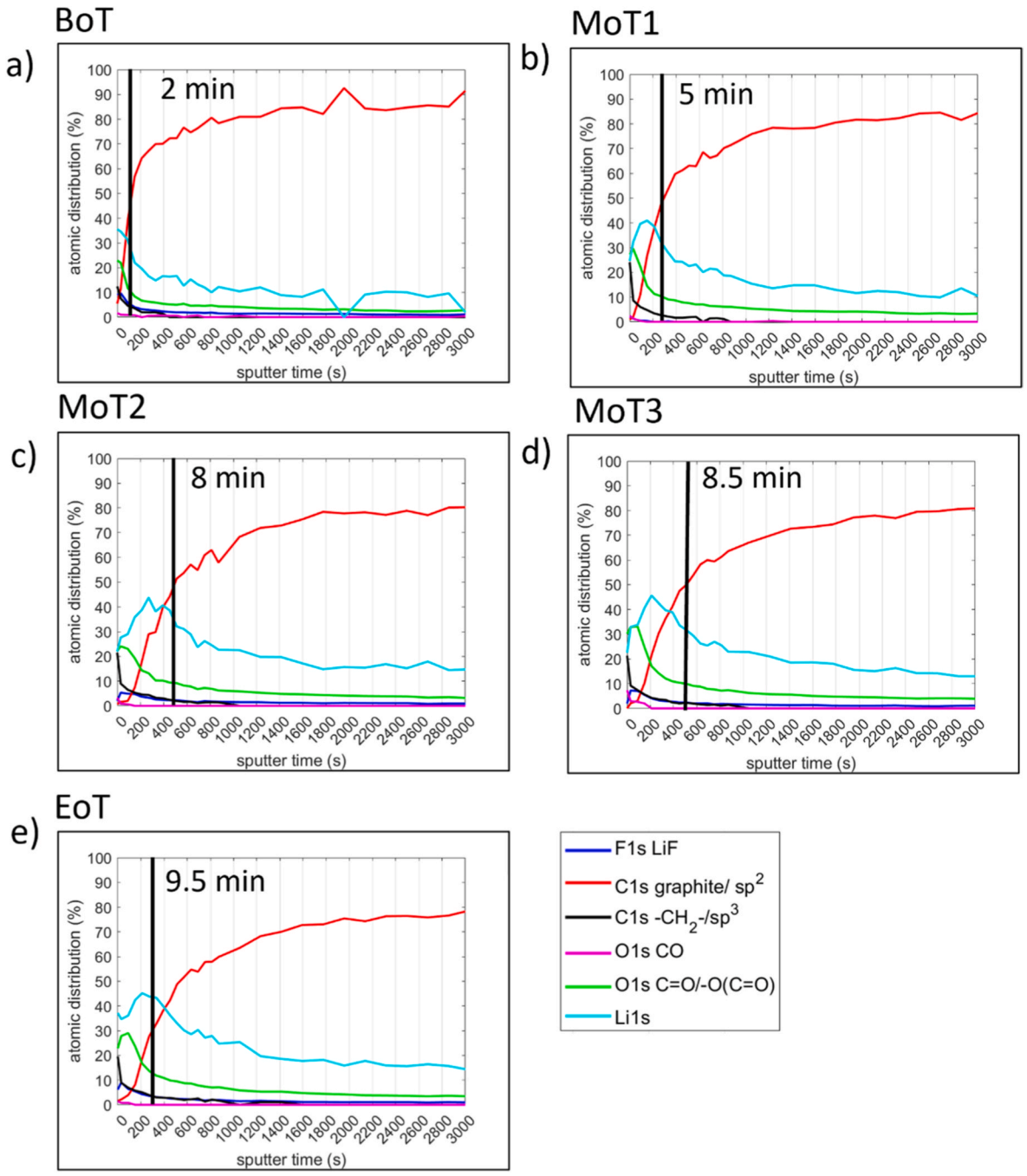

Fig. 4. Sputter depth profiles for selected components in the photoemission spectra of cycle-aged graphite negative electrodes at different SoHs, i.e. BoT (a), MoT1 (b), MoT2, (c), MoT3 (d) and EoT (e). The black vertical line indicates the time the sp^2-C signal has reached an overall content of 50 at.% in the surface layer (cut-off criteria for determining SEI thickness).

agreement with a growing SEI layer, characteristic components, e.g. ethers/alkoxides, carboxylates and carbonates, increase with decreasing state of health. The formation of these organic species is accompanied by a decrease of the lithium concentration at the surface in contact with the electrolyte. In the cell that reached the end-of-life criteria (EoT sample), further degradation processes appear to favor different compounds, leading to a notably altered surface composition.

XPS Sputter Depth Profiling. XPS sputter depth profile analysis was performed using monoatomic Ar^+ etching for samples of all five states of health. The relative elemental distribution of the main SEI constituents in the surface layer on graphite are plotted *vs.* the sputter time in Fig. 4a–e. The corresponding core level spectra for the samples at t = 0 s (no sputtering), were discussed in detail in the previous section. For the sputter profiles in Fig. 4 the surface contents of selected SEI components are shown from the C1s (-CH_2-/sp^3-C), F1s (LiF), O1s (-CO−/−C=O-) and Li1s spectra, as well as the bulk active material peak (graphite/sp^2-C) in the C1s spectrum. In contrast to previous studies, we used specifically the atomic concentration of the bulk sp^2-C signal at 50 at.% as cut-off criteria to estimate the SEI thickness, instead of the total carbon concentration [28,29]. Moreover, the Ar^+-ion-etching rate is calibrated on a Ta_2O_5 reference substrate, which is softer to etch and thus more relatable to the SEI layer than commonly used SiO_2 substrates. Also, the respective etching depth of Ta_2O_5 are indicated by changes in color. Neither of the etching references can fully account for the heterogeneity of the SEI structure. However, this approach should provide a reasonable estimation of the relative changes in surface layer thickness between the samples.

As outlined in the discussion of Fig. 4a–c in the section above, electrode active material is represented by its sp^2-C peak (i.e. the 'bulk' signal). The sp^2-C signal starts out at a comparatively low concentration of 0–5 at.% and increases steeply with increasing sputter time. The atomic concentration reaches a plateau between 80 and 90 at.% after a few hundreds of seconds. With increasing ageing state (from BoT to EoT), the slope of sp^2-C curves reduced gradually. In Fig. 4a–e, the black vertical lines indicate that the sp^2-C concentration has reached 50 at.%. It can be readily seen that the time until the graphite bulk material is reached in the sputter process increased with decreasing state of health. Again, demonstrating that the SEI layer thickness increased over time as well.

In contrast, SEI constituents show an opposite behavior as the surface layer is gradually etched during the sputter process. Their contribution to the overall surface layer content is decreasing with increasing sputter time. The organic fractions of the SEI are represented by the sp^3-C/-CH_2- (unsaturated hydrocarbon) signal in the C1s spectra, as well as the -(C=O)O- (carboxyl) on the signal in the O1s spectra. The sp^3-C/-CH_2- decays rapidly below 5 at.% after less than 200 s of sputtering in the BoT sample (thinnest surface layer). Although the initial decay still proceeds rapidly in samples aged for longer time, it takes notably longer until the content drops below the 5 at.% threshold. This suggests that the fraction of hydrocarbons in the top regions of the SEI was higher than in regions closer to the electrode. Conversely, the -(C=O)O- signals display initial surface contents between 20 and 30 at.% that decay for cycle-aged samples MoT2, and MoT3, as well at the EoT stage (Fig. 4c–e) only after sputter times of 100–200 s. For MoT3 and EoT samples, the carboxylate content first passed a maximum before the signal decayed. The Li1s content followed a similar but more pronounced trend, showing a maximum in the overall Li content that drifted with increasing SoH to higher sputter times. The maximum values are observed after the top layers are removed and both the sp^3-C/-CH_2- and -(C=O)O- contents decayed already to a significant degree. This would fit with the general reports in literature that the SEI tends to be more inorganic in the inner regions [55]. The fraction of inorganic lithium compounds is higher, thus increasing its relative content.

Upon further sputtering, the inner region was removed as well and the bulk signal is the only dominant component. Accordingly, some of the O1s and Li1s signals are maintained over longer sputtering times, indicating the presence of inorganic species. Another reason for the high Li content might be effects of Li plating appearing in samples from MoT2 to EoT, as indicated in Fig. 5 [31]. However, it is important to stress that each of the components discussed herein display different sputtering rates. As a result, inorganic compounds are typically etched significantly slower than organic material and thus accumulate in the remaining surface layer [45]. Moreover, the sputtering process leads to increasing surface roughness, depending on the material distribution and grain sizes that is difficult to predict. In addition, the maximum surface content of sp^2-C at around 80 % (except for BoT) is likely limited, due to residues of electrolyte components and SEI constituents in the electrode porosity and the pores of the graphite active material. A small fraction of the typical SEI components thus remains present during sputter depth profiling. Therefore, complementary electron microscopy techniques are used as additional methods to map the SEI cross-section shown in the following sections.

Electron Microscopy. In this section a compositional analysis was performed of the SEI layer on graphite electrode cross-sections of the MoT1 and EoT cells by scanning electron microscopy (SEM), scanning transmission electron microscopy (STEM) based electron energy loss spectroscopy (EELS) and energy-dispersive X-ray spectroscopy (EDS).

The cross-sections were prepared by a focused ion beam (FIB). Fig. 5a–c shows SEM top view images and Fig. 5d–f FIB-SEM cross sections of the center area of the graphite electrodes. Between the SEM top view images of the graphite surfaces at different ageing states, it is difficult to identify notable morphological differences, although the EoT sample showed signs of particle cracking. The FIB-SEM cross section images show a bright layer on top of the electrode coating that corresponds to a protective Pt/C coating to reduce sputter damage and sample charging. The cross-sections of the BoT, MoT1 and EoT samples (Fig. 5d–f) show large particle size differences between distinct active material particles and an inner porosity. Both in the void space between particles and within the particle microstructure a surface layer and deposits can be observed. Based on the micrographs shown in Fig. 5 the electrode porosity appears to increase in the MoT1 and EoT stage and the microporosity seems increasingly filled with deposited material. In addition, some of the particles in these samples show signs of cracking, as clearly seen in the MoT1 sample to the right. In the EOT sample the particles also appear notably disconnected. However, statistically representative observations, i.e. identifying and distinguishing cutting-/sputter-induced damages from ageing-induced damages, are challenging with this approach due to the small sample size.

The TEM analysis on the FIB-cut lamella is provided in Fig. 6. The annular dark field (ADF) images are shown in the top row of Fig. 6. The EELS/EDS elemental maps are shown below from top to bottom for carbon (red), fluorine (cyan), lithium (green), phosphorous (pink), oxygen (yellow). The EELS elemental map for sulfur is provided in Fig. S4. In addition, the superimposed elemental, maps including all above-mentioned elements except carbon, are provided in the bottom row of Fig. 6 for the evaluation of SEI thicknesses.

The top row shows the corresponding (ADF) images (Fig. 6, top row), showing a bright top section due to the Pt/C coating, and the bulk active material as grey area underneath. As the contrast in ADF scales with atomic number, there is a clear difference between the Pt/C layer and the second period elements Li, C, O and F. However, between second period elements there are only little differences in contrast and hence active material and SEI only display similar grey scales. The location of the SEI becomes clearer in the EELS/EDS elemental maps. In the carbon maps, a strong carbon signal is observed from the bulk graphite particle and a weaker signal from the Pt/C top layer with a small, dark gap between layers. The carbon-lean section in-between rich in homogeneously distributed fluorine, lithium, phosphorous, oxygen and sulfur, and is thus assigned to the SEI layer [33]. In addition, intense signals from Li and O are seen in the pores of the bulk graphite particle. From the superimposed maps, the SEI was estimated as indicated in Fig. 6 (bottom row) by the red arrows, showing layer thicknesses of the center

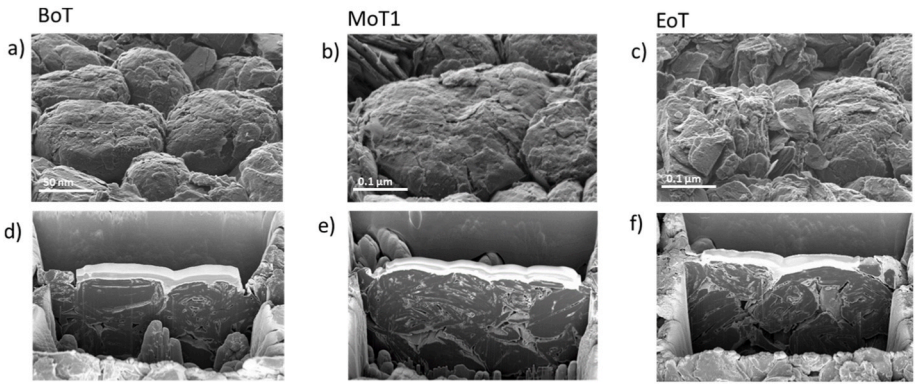

Fig. 5. Top row (a–c): electrode top view SEM micrographs for samples BoT, MoT1, and EoT. bottom row (d–f): FIB-cut electrode cross-sections for the SEI analysis with Pt/C surface coating (bright top layer).

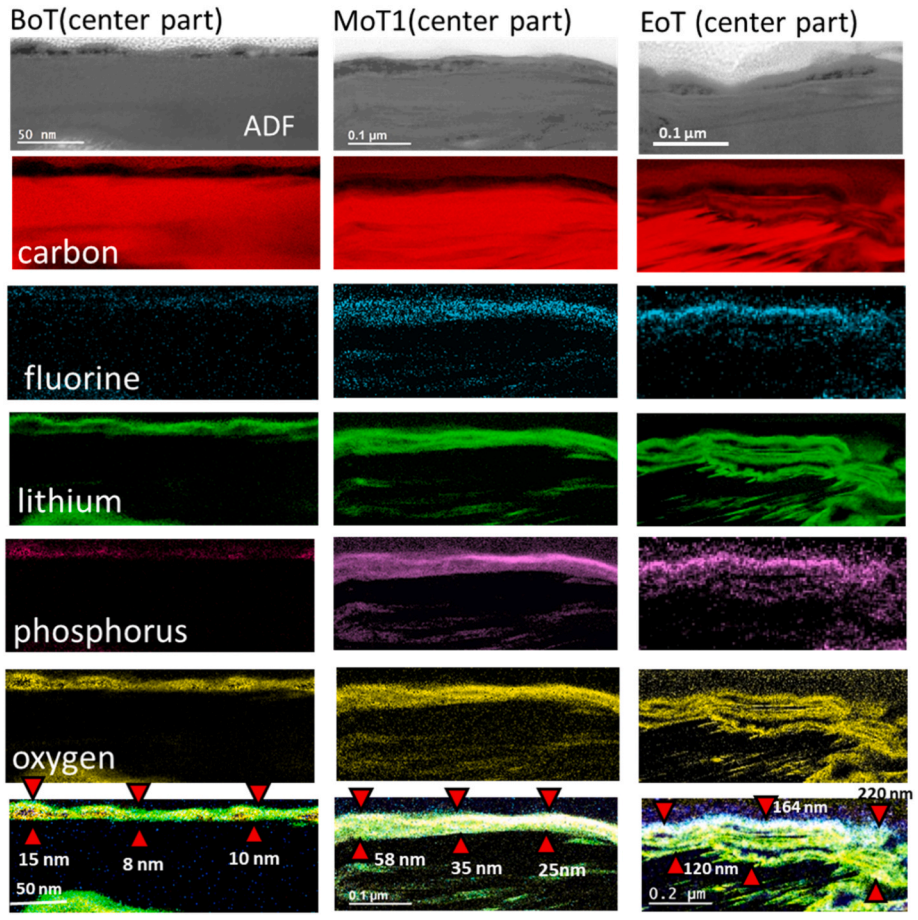

Fig. 6. Annular dark field (ADF) images and corresponding EELS (carbon, lithium and oxygen) and EDS (fluorine and phosphorus) maps of the electrode cross-sections. Estimated SEI growth is pointed out by red arrows which show the SEI layer at minimum and maximum thickness. (For interpretation of the references to color in this figure legend, the reader is referred to the Web version of this article.)

electrode sections around 8–15 nm (BoT), 25–58 nm (MoT1) and 120–220 nm (EoT). It is reported that initially the thickness of the SEI grows rapidly from 50 nm up to 200 nm [22,56]. In comparison the thickness on the edges (Fig. S5) is significantly reduced e.g. ca. 10 nm at MoT1 and ca. 75 nm at EoT. As previously stated, the estimated thickness primarily reflects the central and edge regions, which exhibit notable discrepancies. This is attributed to the heterogeneous distribution of heat, and as a result different degrees of electrolyte degradation, as mentioned previously. While the SEI does attain a specific thickness, it remains overall below the thicknesses determined by the XPS results presented above.

3.2. *Laboratory-scale three-electrode setups from automotive cells*

It was one of the aims in this work, to replicate the ageing of automotive cells in a lab scale setup, which would greatly facilitate the statistics of electrochemical and material analyses and is also deemed safer as compared to handling large format pouch cells. Moreover, the transfer to smaller scales can lead to a significant cost reduction if the ageing behavior can be reproduced.

Therefore, in this last section, an as-received automotive cell was opened to cut and extract smaller electrode discs from anode and cathode sheets. One side of the double-side coated electrodes had to be removed mechanically to fit the three-electrode EL-cell compartment. The challenge on the laboratory cell level is to create similar cell performance in terms of capacity retention, and induce similar degrees of material fatigue at an equivalent charge throughput (eCTP). Fig. 7 shows the capacity retention *vs.* equivalent charge throughput of three three-electrode cells build. For comparison the data of a 43 Ah pouch cell was added as well in this graph. Three of the samples show high reproducibility in their capacity retention with minimal capacity loss. One lab-scale cell (yellow) shows stronger capacity fluctuations in the RPT sequences that could originate from contact problems [57]. In the lab scale setup, a slightly higher capacity retention is observed by about ±1–3 % at 30 °C, compared to the pouch cell after 50 kAh. In general, the lab scale results show slower ageing behavior over the studied charge throughput interval. This is likely due to edge effects in the rectangular electrode sheets of the pouch cell, as compared to circular electrode discs with small diameter and an electrolyte excess. In the latter case the cell reaction (and degradation) across the entire electrode area is more homogenous. Lack of heat dissipation that would lead to accelerated ageing in central cell regions of stacked cells for instance, do not appear to be an issue on this scale. Fresh electrolyte was added in the three-electrode setup to ensure proper cell operation. The active material/electrolyte volume ratio was estimated to be one order of magnitude larger in the lab scale cells than in the automotive cell.

Surface Layer Analysis. As described in the previous sections, the cycle-aged electrodes were subjected to an in-depth analysis using XPS, including a sputter depth profiling analysis, and TEM cross-section analysis, for a comparison of the surface layers of lab-scale and pouch cell.

XPS Analysis. The peak assignment of XPS spectra for the cycle-aged sample (MoT) from the lab-scale cells (Fig. S7) was transferred in good agreement from the MoT1 pouch cell data (Fig. 3) in terms of binding energies (within a margin of less than ±0.2 eV) positions of individual SEI components. Minor changes in the relative peak intensities are observed in the C1s spectrum, especially for instance a smaller relative contribution of the -CO- component. No Li_2O was found in the O1s spectrum, unlike the MoT1 sample (previous section). In addition, the fluoroalkly phosphate species ($O{=}PF_x(OR)_y$) in the F1s spectrum show a smaller intensity relative to the LiF peak. The elemental distribution is provided for comparison in Table 3. BoT sample is the initial point of reference for both aged cell types. The results of the MoT1 sample were also added for comparison. The comparison in relative surface concentrations in Table 3 suggest a significantly larger LiF content of around 31 at.% (compared to 4.8 at.% in MoT1). The remaining 8 at.% is assigned to lithium salts, such as LEDC. Accordingly, the relative fractions of carbonyls in the O1s and C1s spectra is lower in the MoT sample, than in the MoT1 sample. Sputter depth profiling analysis showed a sputter time of 3.5 min (Fig. S6) until the 50 % threshold was reached, placing the estimated SEI thickness between the BoT and MoT1 samples, which is reasonable with respect to the corresponding CTPs (MoT: equivalent CTP = ~50 kAh, MoT1: CTP = ~100 kAh).

TEM cross-section analysis. The EELS/EDS elemental maps are shown in Fig. S8 and display a thin surface layer between 14 and 25 nm in thickness. The results will be further discussed below.

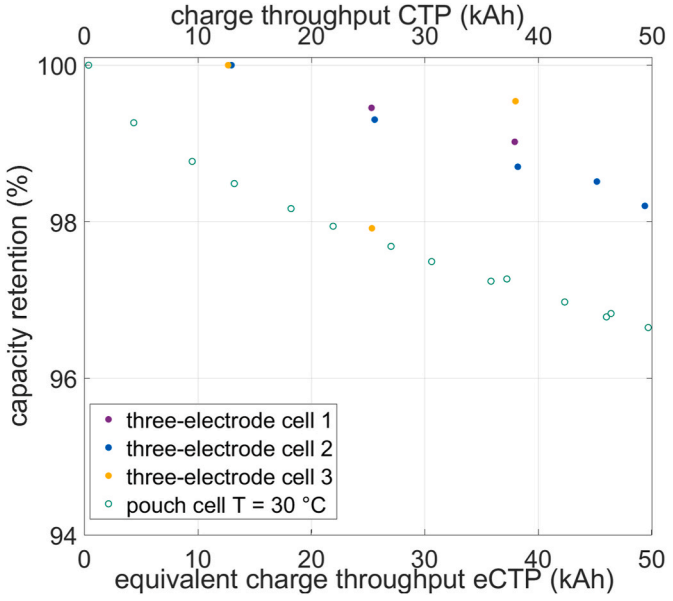

Fig. 7. Capacity retention *vs.* charge throughput (CTP, top x-axis) for three lab-scale three-electrode cells (full circles). For comparison capacity retention of an automotive cell was added from Fig. 2 (*vs.* an equivalent CTP using a conversion factor of 1.5, bottom x-axis). The first RPT check-up of the three-electrode cells was performed at around 12.5 kAh. The reproducibility is validated by the iteration of several test runs and overlapping results of the three-electrode cells.

4. Discussion

Loss of active lithium to SEI layer growth is a major source of capacity fade in batteries. The SEI layer thickness at different stages of ageing is a measure of the growth rate under given operation conditions. Hence, correlating SEI layer properties to electrochemical data is a cornerstone in physics-based models used for lifetime predictions and state-of-health assessments of batteries and is of particular relevance in the automotive sector. The results of this study may serve as a basis for SEI growth rates in aging models that use the initial SEI thickness and the SEI growth rate as parameters, amongst others, to quantify the lithium loss [16]. Both parameters can be determined experimentally by studying the surface layer over the battery lifetime. Herein, we investigated the SEI growth and composition of automotive cells that were cycle-aged in a duty cycling sequence using a custom EV drive profile. The SoH was checked in regular intervals using a reference parameter test to quantify the capacity retention over the entire life span of the cells. The end-of-test criteria was reached when the internal resistance starts increasing significantly. At this point, the capacity retention dropped to 87 % of the initial reference parameters and the internal cell

Table 3
Peak Positions of the C1s, O1s, F1s and P2p regions in the BoT, MoT of the three-electrode cell and MoT1 of the automotive cell. The binding energy boundaries were fixed.

Core Level	Compounds	binding energy	BoT[a]	MoT	MoT1[a]
		eV	at. (%)	at. (%)	at. (%)
C1s	sp [2]-C/graphite	284.4	5.5	0.9	1.0
	$-CH_2-/sp^3$-C	285.0	12.4	10.2	24.0
	-CO-	286.7	1.0	1.6	6.1
	-(C=O)O-	288.9	1.2	1.2	1.6
	-O(C=O)O-	289.9	0.8	0.7	3.4
O1s	Li_2O	528.0	–	–	–
	C=O[b]	531.4	22.9	10.0	27.2
	-CO-	533.3	1.7	1.4	2.5
F1s	LiF	685.0	9.0	30.9	4.8
	$(O{=}P)F_x(OR)_y$	687.4	0.7	1.0	1.9
P2p	$O{=}PF_x(OR)_y$ ($2p_{3/2}$)	133.3	2.3	1.7	1.4
	P-S ($2p_{3/2}$)	132.0	0.7	–	–
Li1s	Li^+	55.4	35.3	38.9	24.5

[a] Added from Table 2 for comparison; The BoT data applies to both cell setups.
[b] C=O (carbonyl groups) include carboxyl groups (-(C=O)O-) and carbonate groups (-O(C=O)O-).

resistance started to notably increase. Additional samples were prepared in lab-scale three-electrode cells with aim to reproduce the performance and ageing behavior of the automotive cells, using the electrode coatings from a disassembled cell stack. This approach could be potentially cheaper and more efficient, than testing larger cell formats.

A detailed surface analysis by X-ray photoelectron spectroscopy on ex-situ samples of different ageing stages showed a gradually growing surface layer. (the sample positions are indicated in Fig. S2). Its thickness exceeded the probing depth of the technique, thus likely excluding (or underestimating) certain SEI components that are most prominent in the 'inner' regions, i.e. close to the electrode, such as LiF. Other characteristic SEI components, particularly carbon-oxygen species, such as carbonates (-O(C=O)O-), carboxyates (-(C=O)O-) or ethers (-CO-), display increasing surface contents from BoT to late MoT conditions. Interestingly, in the P2p spectra only products of the degraded salt were found, fluoroalkyl phosphates ($O{=}PF_x(OR)_y$), but no PF_6^- signal was observed. In addition, P-S bonds, presumably from an electrolyte additive in the proprietary electrolyte were seen in the P2p region.

To quantify the SEI layer growth more accurately at different SoH, the SEI thickness was determined with two different methods, namely XPS sputter depth profiling and EELS/EDS on an electrode cross-section prepared by a focused ion beam. During XPS sputter depth profiling with monoatomic Ar^+ can rapidly lead to a rough surface topology and a preferred edging of the softer, organic components that exhibit a higher sputter rate. Nonetheless, by following the surface concentrations of selected SEI species and the sp^2-C carbon of the graphite active material beneath, it is possible to derive a surface layer thickness from the sputter time, assuming a constant and homogenous sputter rate. For comparison, an SEI/graphite electrode cross-section was characterized by EELS/EDS, which allowed both an elemental contrast and a possibility to measure the SEI thickness from the respective elemental maps. The values extracted from both techniques are summarized in Table 4. The thickness measurements obtained from the XPS as a function of CTP were collected for both the automotive cells and the lab-scale cells (at an equivalent CTP) in Fig. 8a. The as-received large format pouch cells arrived pre-cycled and displayed an initial SEI thickness of ca. 58 nm in the electrode center. In first approximation a SEI growth rate in an ageing model can be derived from a linear fit, yielding a growth rate of 1.1 nm/kAh. However, electrode thicknesses obtained from samples extracted at the edge of the electrode sheets show a slower SEI growth than in the central electrode region (Fig. S9), namely 0.62 nm/kAh. In Fig. 8b the SEI thickness as a function of CTP were derived from TEM cross-section analysis. The data also follows in first approximation a linear growth rate of 0.32 nm/kAh. With regard to the edge parts, the SEI growth rate at 0.11 nm/kAh, which is therefore lower than to the center (Fig. S9). The EoT sample (center) appears to break with the trend, which is consistent with changes in the SEI composition and was not considered in the linear fit.

Therefore, our results highlight that the SEI growth rate depends strongly on the technique used to determine the SEI thickness after different ageing states, and, for larger format cells, also on the location on the electrode sheet from which the sample is extracted. In addition, gradients in SEI thicknesses are highly likely across a cell stack. The results clearly demonstrate a high level of non-uniform ageing on an electrode sheet, which is associated for instance to temperature gradients during cycling across the electrode. Although our two approaches yielded notably different growth rates, we demonstrated that both approaches displayed a linear relationship (in first approximation) between SEI layer growth and ageing time, provided that sufficient amounts of electrolyte were present. Signs of electrolyte dry out and considerable deviations from the linear SEI thickness growth, as well as SEI composition, were only observed in EoT samples. Even though the SEI composition differed markedly between automotive (stacked) cells and labscale three-electrode cells, their ageing behavior appeared to fit seemingly into the linear ageing trends/SEI layer thicknesses presented in Fig. 8 (a normalization of the CTP was necessary to bridge the scales of the two cell setups). Although notable differences were observed in the surface layer compositions of pouch and lab-scale cells, their SEI growth rates appeared comparable nonetheless. Therefore, experimental data on the SEI growth rate from lab-scale-built cells could be a viable alternative to testing large-format pouch cells, enabling the acquisition of statistically relevant sample sizes with better reproducibility. Moreover, sources of error resulting from non-uniformities of large electrode areas, such as poor heat dissipation, can be effectively eliminated in smaller setups. The non-uniform ageing of the electrodes will likely continue to present a challenge in accurately predicting the ageing of an entire cell stack. However, it is clearly an influential factor in lifetime predictions.

Table 4
Summary of the estimated quantification of the SEI growth measured by XPS and EELS/EDS of the three-electrode and automotive cells. The images of EELS/EDS on the SEI of the three-electrode cell is shown in Fig. S8. The range of measured surface layer thicknesses from EELS/EDS measurements is shown in Fig. S10. The thickness measurement for the BoT was taken at the center, assuming a homogenous distribution. The samples of MoT2 were not analyzed by EELS/EDS.

Method	Position	Measured Surface Layer Thickness/nm					
		BoT	MoT	MoT1	MoT2	MoT3	EoT
XPS	center	58	109	144	250	265	296
EELS/EDS	center	10	20	39		73	168
EELS/EDS deviation	min/max	8/15	14/25	25/5		69/77	50/100
XPS	edge			140	130	200	266
EELS/EDS	edge			10		33	75
EELS/EDS deviation	min/max			9/12		21/45	30/65

5. Conclusions

Data-driven approaches to battery lifetime predictions require experimental input parameters such as the SEI growth rate. Herein, changes in SEI thickness of cycle-aged electrodes from automotive or lab-scale three-electrode cells are determined by two different approaches, namely X-ray photoelectron spectroscopy sputter depth profiling and electron microscopy using elemental mapping of electrode cross-sections. Both approaches suggest a linear SEI growth rate with increasing ageing time but display significantly different absolute growth rates. The results further demonstrated that the SEI thickness is non-uniform on larger electrode sheets with considerable differences in layer thickness between edge and center areas of the electrode. Notable deviations from the linear behavior was only observed at the end of cell life, when the cell showed signs of electrolyte dry out. In an attempt to reduce the number of larger format cells in cycle-ageing tests, a lab-scale setup was developed from automotive cell components that could reproduce the trends in SEI growth, even though XPS analysis suggested different SEI compositions between surface layers formed on negative electrodes from automotive cells and lab-scale three-electrode cells. Hence, this approach can potentially facilitate sample testing and improve sampling statistics, thus providing easier access to SEI growth rates for a data-driven ageing model. While the general tends (such as a linear SEI growth rate) should be transferable to other cell configurations, there are likely strong differences in absolute numbers in dependence of electrode compositions, separator materials and cell formats.

CRediT authorship contribution statement

Franziska Allgayer: Writing – original draft, Visualization, Validation, Methodology, Investigation, Data curation, Conceptualization. **Markus H. Hofmann:** Writing – review & editing, Methodology, Conceptualization. **Helmut Ehrenberg:** Writing – review & editing. **Mathias Storch:** Writing – review & editing, Methodology,

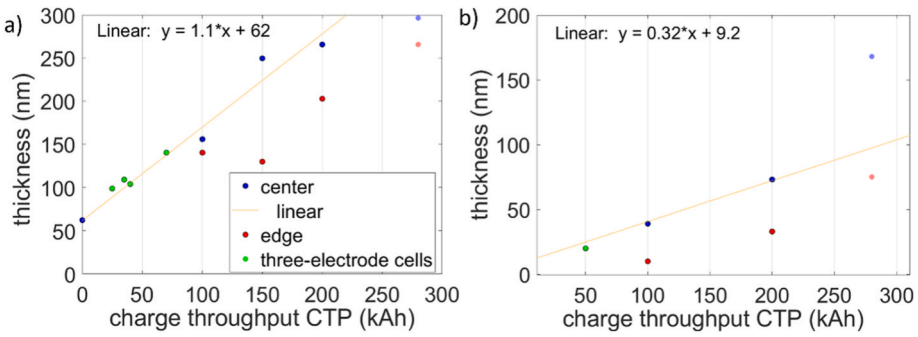

Fig. 8. SEI thicknesses for automotive and lab-scale samples as a function of different charge throughput (CTP) for measurements performed in the center (blue dots) and at the edge regions (red dots) of differently aged electrode samples. In a) the thickness was derived from XPS sputter depth profiling after reaching the 50 at. %/sp^2-C threshold, as shown in Fig. 4. In b) the thickness was derived from EELS/EDS measurements and mapped to estimate the SEI growth, as indicated in Fig. 6 with the red arrows for maximum and minimum thicknesses. The linear fits in a) and b) refer to the center parts of the electrode layer. (For interpretation of the references to color in this figure legend, the reader is referred to the Web version of this article.)

Conceptualization. **Fabian Jeschull:** Writing – review & editing, Writing – original draft, Methodology, Conceptualization.

Declaration of generative AI use

During the preparation of this work the author(s) used *DeepL Write* in order to spellcheck and edit the manuscript. After using this tool, the authors reviewed and edited the content as needed and take full responsibility for the content of the published article.

Declaration of competing interest

The authors declare that they have no known competing financial interests or personal relationships that could have appeared to influence the work reported in this paper.

Acknowledgements

This work contributes to the research performed at CELEST (Center for Electrochemical Energy Storage Ulm-Karlsruhe, Germany). The authors acknowledge the financial support of Mercedes-Benz AG, (Stuttgart, Germany). We would also like to thank our colleagues from Mercedes-Benz AG for the support during analysis and for sharing their knowledge with us. As well the colleagues from KIT to support the XPS analysis.

Appendix A. Supplementary data

Supplementary data to this article can be found online at https://doi.org/10.1016/j.jpowsour.2025.239053.

Data availability

The data that has been used is confidential.

References

[1] A. Barré, B. Deguilhem, S. Grolleau, M. Gérard, F. Suard, D. Riu, A review on lithium-ion battery ageing mechanisms and estimations for automotive applications, J. Power Sources 241 (2013) 680–689, https://doi.org/10.1016/j.jpowsour.2013.05.040.

[2] J. Klemens, A. Wurba, D. Burger, M. Müller, W. Bauer, S. Büchele, O. Leonet, J. A. Blázquez, I. Boyano, E. Ayerbe, H. Ehrenberg, J. Fleischer, A. Smith, P. Scharfer, W. Schabel, Challenges and opportunities for large-scale electrode processing for sodium-ion and lithium-ion battery, Batter. Supercaps 6 (11) (2023) e202300291, https://doi.org/10.1002/batt.202300291.

[3] W. Bauer, Special features of powder technology for the production of lithium-ion batteries, Interceram. - Int. Ceram. Rev. 68 (4) (2019) 18–21, https://doi.org/10.1007/s42411-019-0014-y.

[4] Jeschull, F.; Maibach, J.; Félix, R.; Wohlfahrt-Mehrens, M.; Edström, K.; Memm, M.; Brandell, D. Solid electrolyte interphase (SEI) of water-processed graphite electrodes examined in a 65 mAh full cell configuration. ACS Appl. Energy Mater. 2018, acsaem.8b00608. https://doi.org/10.1021/acsaem.8b00608..

[5] M. Klett, J.A. Gilbert, K.Z. Pupek, S.E. Trask, D.P. Abraham, Layered oxide, graphite and silicon-graphite electrodes for lithium-ion cells: effect of electrolyte composition and cycling windows, J. Electrochem. Soc. 164 (1) (2017) A6095–A6102, https://doi.org/10.1149/2.0131701jes.

[6] A. Smith, P. Stüble, L. Leuthner, A. Hofmann, F. Jeschull, L. Mereacre, Potential and limitations of research battery cell types for electrochemical data acquisition, Batter. Supercaps 6 (6) (2023) e202300080, https://doi.org/10.1002/batt.202300080.

[7] T. Waldmann, M. Wilka, M. Kasper, M. Fleischhammer, M. Wohlfahrt-Mehrens, Temperature dependent ageing mechanisms in lithium-ion batteries – a post-mortem study, J. Power Sources 262 (2014) 129–135, https://doi.org/10.1016/j.jpowsour.2014.03.112.

[8] C. Schmitt, D. Kopljar, K.A. Friedrich, Detailed investigation of degradation modes and mechanisms of a cylindrical high-energy Li-Ion cell cycled at different temperatures, J. Energy Storage 120 (2025) 116486, https://doi.org/10.1016/j.est.2025.116486.

[9] M. Ecker, N. Nieto, S. Käbitz, J. Schmalstieg, H. Blanke, A. Warnecke, D.U. Sauer, Calendar and cycle life study of Li(NiMnCo)O2-Based 18650 lithium-ion batteries, J. Power Sources 248 (2014) 839–851, https://doi.org/10.1016/j.jpowsour.2013.09.143.

[10] M. Lewerenz, D.U. Sauer, Evaluation of cyclic aging tests of prismatic automotive LiNiMnCoO2-Graphite cells considering influence of homogeneity and anode overhang, J. Energy Storage 18 (2018) 421–434, https://doi.org/10.1016/j.est.2018.06.003.

[11] J. Stadler, T.K. Groch, M. García, M. Storch, J. Fath, M. Ecker, A. Latz, Comprehensive analysis of lithium-ion cells and heir aging trajectory toward nonlinear aging, J. Energy Storage 65 (2023) 107247, https://doi.org/10.1016/j.est.2023.107247.

[12] J. Stadler, C. Krupp, M. Ecker, J. Bandlow, B. Spier, A. Latz, Investigation and modeling of cyclic aging using a design of experiment with automotive grade lithium-ion cells, J. Power Sources 521 (2022) 230952, https://doi.org/10.1016/j.jpowsour.2021.230952.

[13] S. Paarmann, M. Schreiber, A. Chahbaz, F. Hildenbrand, G. Stahl, M. Rogge, P. Dechent, O. Queisser, S.D. Frankl, P. Morales Torricos, Y. Lu, N.I. Nikolov, M. Kateri, D.U. Sauer, M.A. Danzer, T. Wetzel, C. Endisch, M. Lienkamp, A. Jossen, M. Lewerenz, Short-term tests, long-term predictions – accelerating ageing characterisation of lithium-ion batteries, Batter. Supercaps 7 (11) (2024) e202300594, https://doi.org/10.1002/batt.202300594.

[14] M. Schreiber, K. Abo Gamra, P. Bilfinger, O. Teichert, J. Schneider, T. Kröger, N. Wassiliadis, M. Ank, M. Rogge, J. Schöberl, P. Rosner, C. Grosu, A. Jossen, M. Lienkamp, Understanding lithium-ion battery degradation in vehicle applications: insights from realistic and accelerated aging tests using volkswagen ID.3 pouch cells, J. Energy Storage 112 (2025) 115357, https://doi.org/10.1016/j.est.2025.115357.

[15] P.M. Attia, A. Bills, F. Brosa Planella, P. Dechent, G. Dos Reis, M. Dubarry, P. Gasper, R. Gilchrist, S. Greenbank, D. Howey, O. Liu, E. Khoo, Y. Preger, A. Soni, S. Sripad, A.G. Stefanopoulou, V. Sulzer, Review—"Knees" in lithium-ion battery aging trajectories, J. Electrochem. Soc. 169 (6) (2022) 060517, https://doi.org/10.1149/1945-7111/ac6d13.

[16] L. Von Kolzenberg, J. Stadler, J. Fath, M. Ecker, B. Horstmann, A. Latz, A four parameter model for the solid-electrolyte interphase to predict battery aging during operation, J. Power Sources 539 (2022) 231560, https://doi.org/10.1016/j.jpowsour.2022.231560.

[17] *IEEE Guide for Control Architecture for High Power Electronics (1 MW and Greater) Used in Electric Power Transmission and Distribution Systems*; Institute of Electrical and Electronics Engineers, IEEE-SA Standards Board, Institute of Electrical and Electronics Engineers, New York, 2011.

[18] A. Barré, B. Deguilhem, S. Grolleau, M. Gérard, F. Suard, D. Riu, A review on lithium-ion battery ageing mechanisms and estimations for automotive applications, J. Power Sources 241 (2013) 680–689, https://doi.org/10.1016/j.jpowsour.2013.05.040.
[19] V.A. Agubra, J.W. Fergus, The formation and stability of the solid electrolyte interface on the graphite anode, J. Power Sources 268 (2014) 153–162, https://doi.org/10.1016/j.jpowsour.2014.06.024.
[20] V. Agubra, J. Fergus, Lithium ion battery anode aging mechanisms, Materials 6 (4) (2013) 1310–1325, https://doi.org/10.3390/ma6041310.
[21] P. Verma, P. Maire, P. Novák, A review of the features and analyses of the solid electrolyte interphase in Li-Ion batteries, Electrochim. Acta 55 (22) (2010) 6332–6341, https://doi.org/10.1016/j.electacta.2010.05.072.
[22] V.R. Rikka, S.R. Sahu, A. Chatterjee, P.V. Satyam, R. Prakash, M.S.R. Rao, R. Gopalan, G. Sundararajan, In Situ/Ex situ investigations on the formation of the mosaic solid electrolyte interface layer on graphite anode for lithium-ion batteries, J. Phys. Chem. C 122 (50) (2018) 28717–28726, https://doi.org/10.1021/acs.jpcc.8b09210.
[23] M.B. Pinson, M.Z. Bazant, Theory of SEI formation in rechargeable batteries: capacity fade, accelerated aging and lifetime prediction, arXiv (2012), https://doi.org/10.48550/ARXIV.1210.3672.
[24] J. De Hoog, T. Alpcan, M. Brazil, D.A. Thomas, I. Mareels, Optimal charging of electric vehicles taking distribution network constraints into account, IEEE Trans. Power Syst. 30 (1) (2015) 365–375, https://doi.org/10.1109/TPWRS.2014.2318293.
[25] T.C. Bach, S.F. Schuster, E. Fleder, J. Müller, M.J. Brand, H. Lorrmann, A. Jossen, G. Sextl, Nonlinear aging of cylindrical lithium-ion cells linked to heterogeneous compression, J. Energy Storage 5 (2016) 212–223, https://doi.org/10.1016/j.est.2016.01.003.
[26] M. Ecker, P. Shafiei Sabet, D.U. Sauer, Influence of operational condition on lithium plating for commercial lithium-ion batteries – electrochemical experiments and post-mortem-analysis, Appl. Energy 206 (2017) 934–946, https://doi.org/10.1016/j.apenergy.2017.08.034.
[27] S. Gantenbein, M. Schönleber, M. Weiss, E. Ivers-Tiffée, Capacity fade in lithium-ion batteries and cyclic aging over various state-of-charge ranges, Sustainability 11 (23) (2019) 6697, https://doi.org/10.3390/su11236697.
[28] K. Edström, M. Herstedt, D.P. Abraham, A new look at the solid electrolyte interphase on graphite anodes in Li-Ion batteries, J. Power Sources 153 (2) (2006) 380–384, https://doi.org/10.1016/j.jpowsour.2005.05.062.
[29] V. Eshkenazi, E. Peled, L. Burstein, D. Golodnitsky, XPS analysis of the SEI formed on carbonaceous materials, Solid State Ionics 170 (1–2) (2004) 83–91, https://doi.org/10.1016/S0167-2738(03)00107-3.
[30] K. Ciosek Högström, S. Malmgren, M. Hahlin, M. Gorgoi, L. Nyholm, H. Rensmo, K. Edström, The buried carbon/solid electrolyte interphase in Li-Ion batteries studied by hard X-Ray photoelectron spectroscopy, Electrochim. Acta 138 (2014) 430–436, https://doi.org/10.1016/j.electacta.2014.06.129.
[31] B.T. Young, D.R. Heskett, C.C. Nguyen, M. Nie, J.C. Woicik, B.L. Lucht, Hard X-Ray photoelectron spectroscopy (HAXPES) investigation of the silicon solid electrolyte interphase (SEI) in lithium-ion batteries, ACS Appl. Mater. Interfaces 7 (36) (2015) 20004–20011, https://doi.org/10.1021/acsami.5b04845.
[32] X. Zhou, G.E. Thompson, Electron and photon based spatially resolved techniques, in: Reference Module in Materials Science and Materials Engineering, Elsevier, 2017, https://doi.org/10.1016/B978-0-12-803581-8.10140-7. B9780128035818101407.
[33] K. He, TEM characterization of battery materials, in: Encyclopedia of Energy Storage, Elsevier, 2022, pp. 256–264, https://doi.org/10.1016/B978-0-12-819723-3.00084-6.
[34] Y. Liu, Q. Li, Z. Wang, Recent progress about transmission electron microscopy characterizations on lithium-ion batteries, J. Energy Chem. 95 (2024) 39–56, https://doi.org/10.1016/j.jechem.2024.03.035.
[35] J. Stadler, T.K. Groch, M. García, M. Storch, J. Fath, M. Ecker, A. Latz, Comprehensive analysis of lithium-ion cells and their aging trajectory toward nonlinear aging, J. Energy Storage 65 (2023) 107247, https://doi.org/10.1016/j.est.2023.107247.
[36] T. Roth, L. Streck, N. Mujanovic, M. Winter, P. Niehoff, A. Jossen, Transient self-discharge after formation in lithium-ion cells: impact of state-of-charge and anode overhang, J. Electrochem. Soc. 170 (8) (2023) 080524, https://doi.org/10.1149/1945-7111/acf164.
[37] J. Stadler, C. Krupp, M. Ecker, J. Bandlow, B. Spier, A. Latz, Investigation and modeling of cyclic aging using a design of experiment with automotive grade lithium-ion cells, J. Power Sources 521 (2022) 230952, https://doi.org/10.1016/j.jpowsour.2021.230952.
[38] J. Sieg, M. Storch, J. Fath, A. Nuhic, J. Bandlow, B. Spier, D.U. Sauer, Local degradation and differential voltage analysis of aged lithium-ion pouch cells, J. Energy Storage 30 (2020) 101582, https://doi.org/10.1016/j.est.2020.101582.
[39] T. Waldmann, A. Iturrondobeitia, M. Kasper, N. Ghanbari, F. Aguesse, E. Bekaert, L. Daniel, S. Genies, I.J. Gordon, M.W. Löble, E. De Vito, M. Wohlfahrt-Mehrens, Review—post-mortem analysis of aged lithium-ion batteries: disassembly methodology and physico-chemical analysis techniques, J. Electrochem. Soc. 163 (10) (2016) A2149–A2164, https://doi.org/10.1149/2.1211609jes.
[40] I. Bloom, A.N. Jansen, D.P. Abraham, J. Knuth, S.A. Jones, V.S. Battaglia, G. L. Henriksen, Differential voltage analyses of high-power, lithium-ion cells, J. Power Sources 139 (1–2) (2005) 295–303, https://doi.org/10.1016/j.jpowsour.2004.07.021.
[41] J. Zhu, M.S. Dewi Darma, M. Knapp, D.R. Sørensen, M. Heere, Q. Fang, X. Wang, H. Dai, L. Mereacre, A. Senyshyn, X. Wei, H. Ehrenberg, Investigation of lithium-ion battery degradation mechanisms by combining differential voltage analysis and alternating current impedance, J. Power Sources 448 (2020) 227575, https://doi.org/10.1016/j.jpowsour.2019.227575.
[42] J.P. Fath, D. Dragicevic, L. Bittel, A. Nuhic, J. Sieg, S. Hahn, L. Alsheimer, B. Spier, T. Wetzel, Quantification of aging mechanisms and inhomogeneity in cycled lithium-ion cells by differential voltage analysis, J. Energy Storage 25 (2019) 100813, https://doi.org/10.1016/j.est.2019.100813.
[43] K. Xu, Nonaqueous liquid electrolytes for lithium-based rechargeable batteries, Chem. Rev. 104 (10) (2004) 4303–4418, https://doi.org/10.1021/cr030203g.
[44] H.M. Dahn, A.J. Smith, J.C. Burns, D.A. Stevens, J.R. Dahn, User-friendly differential voltage analysis freeware for the analysis of degradation mechanisms in Li-Ion batteries, J. Electrochem. Soc. 159 (9) (2012) A1405–A1409, https://doi.org/10.1149/2.013209jes.
[45] T. Yoshida, M. Takahashi, S. Morikawa, C. Ihara, H. Katsukawa, T. Shiratsuchi, J. Yamaki, Degradation mechanism and life prediction of lithium-ion batteries, J. Electrochem. Soc. 153 (3) (2006) A576, https://doi.org/10.1149/1.2162467.
[46] S. Kosch, A. Rheinfeld, S.V. Erhard, A. Jossen, An extended polarization model to study the influence of current collector geometry of large-format lithium-ion pouch cells, J. Power Sources 342 (2017) 666–676, https://doi.org/10.1016/j.jpowsour.2016.12.110.
[47] A. Shellikeri, V. Watson, D. Adams, E.E. Kalu, J.A. Read, T.R. Jow, J.S. Zheng, J. P. Zheng, Investigation of pre-lithiation in graphite and hard-carbon anodes using different lithium source structures, J. Electrochem. Soc. 164 (14) (2017) A3914–A3924, https://doi.org/10.1149/2.1511714jes.
[48] M. Storch, S.L. Hahn, J. Stadler, R. Swaminathan, D. Vrankovic, C. Krupp, R. Riedel, Post-mortem analysis of calendar aged large-format lithium-ion cells: investigation of the solid electrolyte interphase, J. Power Sources 443 (2019) 227243, https://doi.org/10.1016/j.jpowsour.2019.227243.
[49] D. Bar-Tow, E. Peled, L. Burstein, A study of highly oriented pyrolytic graphite as a model for the graphite anode in li-ion batteries, J. Electrochem. Soc. 146 (3) (1999) 824–832, https://doi.org/10.1149/1.1391688.
[50] B.S. Parimalam, A.D. MacIntosh, R. Kadam, B.L. Lucht, Decomposition reactions of anode solid electrolyte interphase (SEI) components with $LiPF_6$, J. Phys. Chem. C 121 (41) (2017) 22733–22738, https://doi.org/10.1021/acs.jpcc.7b08433.
[51] S.K. Heiskanen, J. Kim, B.L. Lucht, Generation and evolution of the solid electrolyte interphase of lithium-ion batteries, Joule 3 (10) (2019) 2322–2333, https://doi.org/10.1016/j.joule.2019.08.018.
[52] S.F. Lux, J. Chevalier, I.T. Lucas, R. Kostecki, HF formation in LiPF6-Based organic carbonate electrolytes, ECS Electrochem. Lett. 2 (12) (2013) A121–A123, https://doi.org/10.1149/2.005312eel.
[53] B. Tong, Z. Song, H. Wan, W. Feng, M. Armand, J. Liu, H. Zhang, Z. Zhou, Sulfur-containing compounds as electrolyte additives for lithium-ion batteries, InfoMat 3 (12) (2021) 1364–1392, https://doi.org/10.1002/inf2.12235.
[54] F. Allgayer, J. Maibach, F. Jeschull, Comparing the solid electrolyte interphases on graphite electrodes in K and Li Half cells, ACS Appl. Energy Mater. 5 (1) (2022) 1136–1148, https://doi.org/10.1021/acsaem.1c03491.
[55] S. Malmgren, K. Ciosek, M. Hahlin, T. Gustafsson, M. Gorgoi, H. Rensmo, K. Edström, Comparing anode and cathode electrode/electrolyte interface composition and morphology using soft and hard X-Ray photoelectron spectroscopy, Electrochim. Acta 97 (2013) 23–32, https://doi.org/10.1016/j.electacta.2013.03.010.
[56] S.K. Heiskanen, J. Kim, B.L. Lucht, Generation and evolution of the solid electrolyte interphase of lithium-ion batteries, Joule 3 (10) (2019) 2322–2333, https://doi.org/10.1016/j.joule.2019.08.018.
[57] A.U. Schmid, A. Ridder, M. Hahn, K. Schofer, K.P. Birke, Aging of extracted and reassembled Li-Ion electrode material in coin cells—capabilities and limitations, Batteries 6 (2) (2020) 33, https://doi.org/10.3390/batteries6020033.